Cell Reports Physical Science, Volume *1*

Supplemental Information

Complete Reconstruction of Hydrate Pre-Catalysts for Ultrastable Water Electrolysis in Industrial-Concentration Alkali Media

Xiong Liu, Jiashen Meng, Kun Ni, Ruiting Guo, Fanjie Xia, Jingjing Xie, Xu Li, Bo Wen, Peijie Wu, Ming Li, Jinsong Wu, Xiaojun Wu, Liqiang Mai, and Dongyuan Zhao

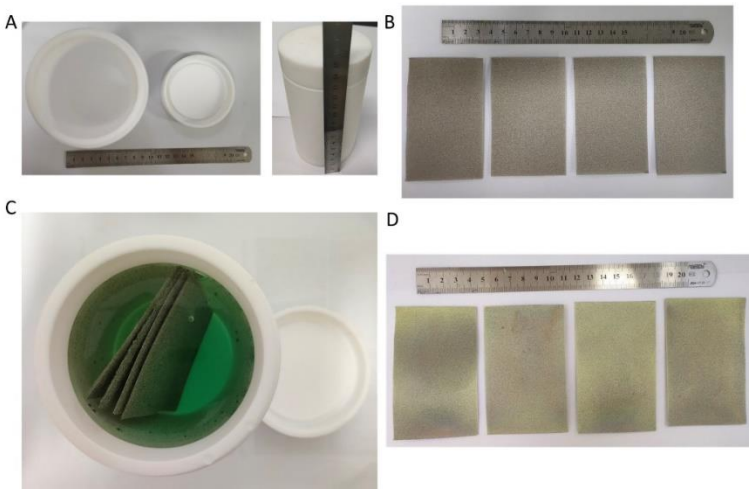

Figure S1. (A) Optical photo of 500 mL Teflon-lined autoclave for mass production. (B, C) Optical photo of four pieces of nickel foams for one-pot synthesis. (D) Optical photo of four pieces of $NiMoO_4 \cdot xH_2O$ NWs/NF after one-time synthesis.

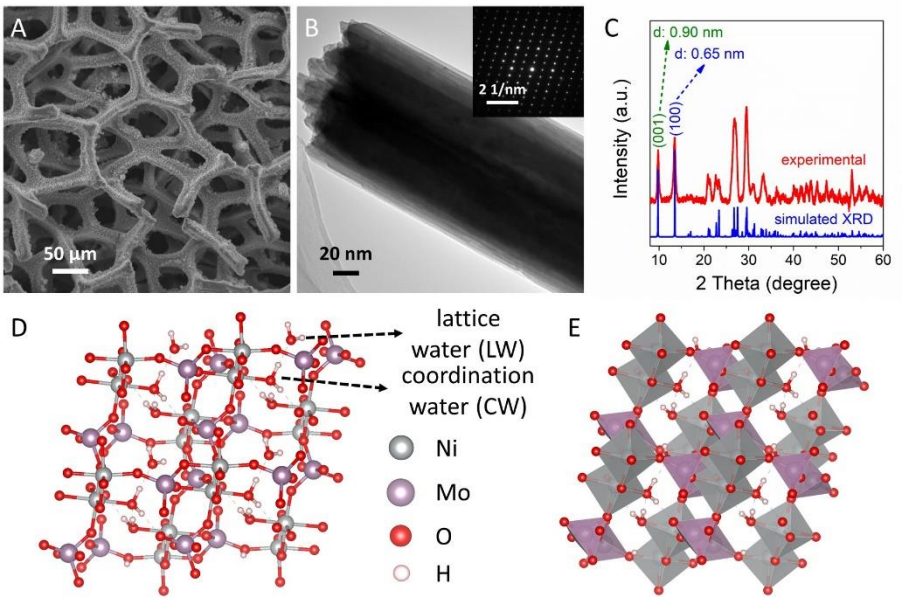

Figure S2. (A) SEM image of $NiMoO_4 \cdot xH_2O$ NWs/NF. (B) TEM image of a single $NiMoO_4 \cdot xH_2O$ nanowire. The inset in (B) is the corresponding SAED pattern. (C) XRD pattern of $NiMoO_4 \cdot xH_2O$ nanowires and the simulated XRD based on the optimized $NiMoO_4 \cdot 0.75H_2O$ crystal structure. (D, E) Crystal structures of $NiMoO_4 \cdot 0.75H_2O$, containing MoO_4 tetrahedra, NiO_6 octahedra, lattice water (LW) and coordination water (CW).

As a result, the simulated crystal structure of $NiMoO_4 \cdot xH_2O$ shows a triclinic cell with

parameters of a=6.82 Å, b=6.91 Å, c=9.34 Å, α=76.19°, β=83.85°, γ=74.04°. This hydrate consists of MoO_4 tetrahedra, NiO_6 octahedra, coordination water which shares the O atom with NiO_6 as well as lattice water which has no direct connection to other atoms. The z-shaped $[NiO_6]_4$ units, which consist of four edge-shared NiO_6 octahedra, are linked with MoO_4 tetrahedra to form the three-dimensional network. Based on the optimized crystal structure, the calculated XRD pattern matches well with that of the as-prepared $NiMoO_4 \cdot xH_2O$ powder, which demonstrates the rationality of $NiMoO_4 \cdot 0.75H_2O$.

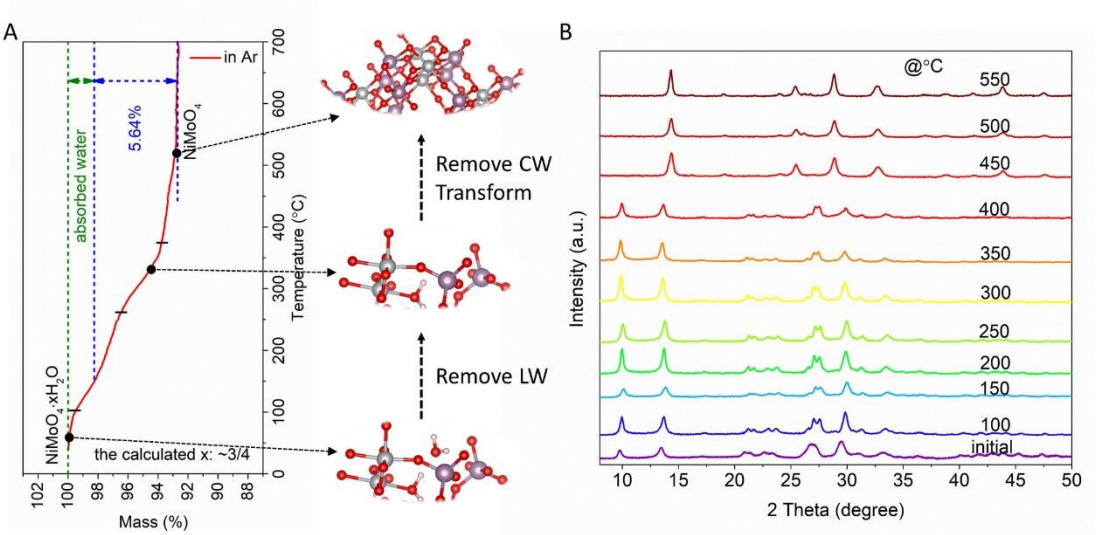

Figure S3. (A) TG curve of the $NiMoO_4 \cdot xH_2O$ powder and its transformation to $NiMoO_4$. (B) Ex situ XRD patterns of $NiMoO_4 \cdot xH_2O$ calcined at different temperatures, showing that the $NiMoO_4 \cdot xH_2O$ can transform to $NiMoO_4$ when the calcined temperature is higher than 400°C.

Figure S3A depicts thermogravimetric analysis curve of $NiMoO_4 \cdot xH_2O$ powder and corresponding structural transformation from $NiMoO_4 \cdot xH_2O$ to $NiMoO_4$. The dehydration trend displays three stages including the loss of absorbed water, the gradual release of lattice water (LW) and the abrupt exclusion of coordination water (CW), which is consistent with the dehydration of $CoMoO_4 \cdot 0.75H_2O$. The mass loss of 5.64 wt.% indicates 1 mol $NiMoO_4 \cdot xH_2O$ contains approximately 0.75 mol crystal water molecules, which supports the formula of the calculated one.

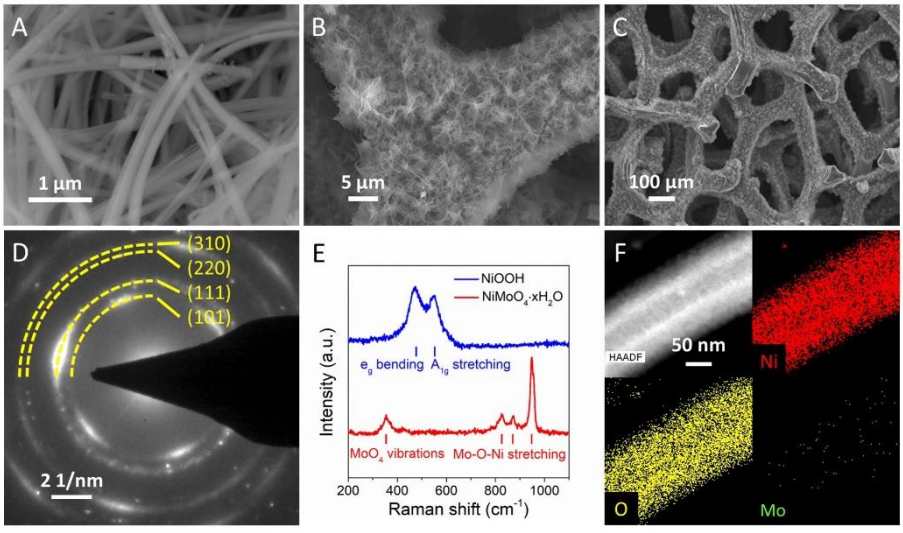

Figure S4. (A-C) SEM images, and (D) SAED pattern of CR-NiOOH. (E) Raman spectra of $NiMoO_4 \cdot xH_2O$ and its derived CR-NiOOH. (F) HAADF STEM image and corresponding elemental mappings of a single CR-NiOOH nanowire.

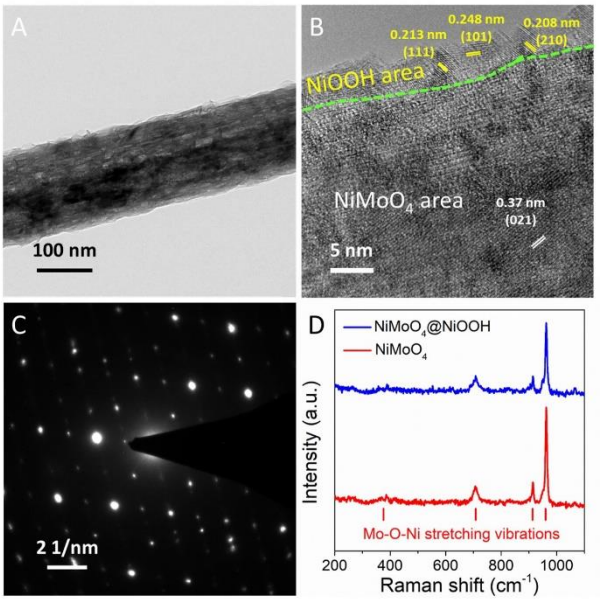

Figure S5. (A) TEM, (B) HRTEM images, and (C) SAED pattern of core-shell $NiMoO_4$@NiOOH derived from $NiMoO_4$ nanowires. (D) Raman spectra of $NiMoO_4$ and its derived $NiMoO_4$@NiOOH.

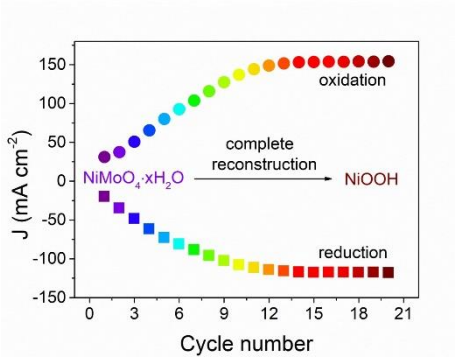

Figure S6. Relationship between the current densities of redox peaks and CV cycles.

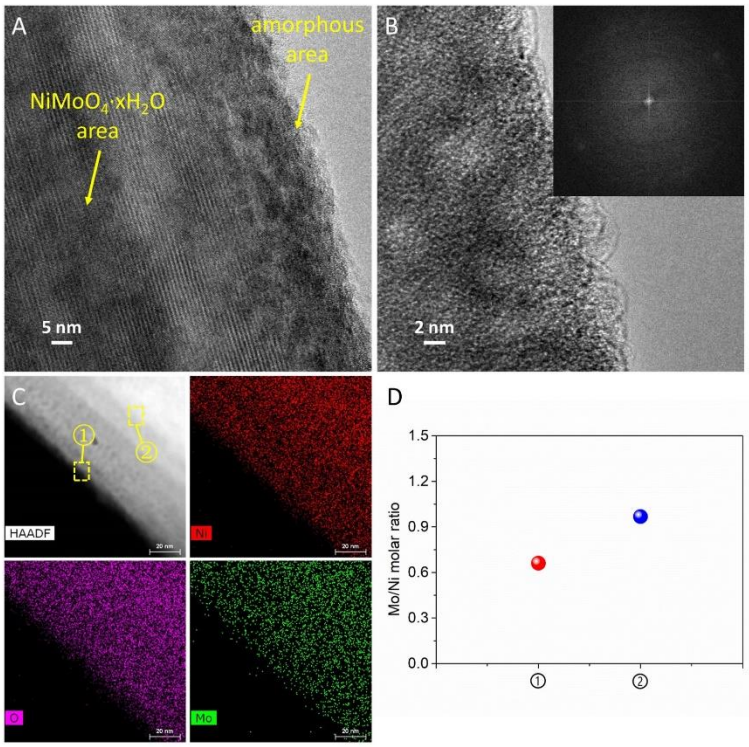

Figure S7. Characterizations on the intermediate product after first-CV cycle to 1.23 V_{RHE} based on $NiMoO_4 \cdot xH_2O$ nanowires (also see in Figure 3D). (A, B) TEM and HRTEM images. The inset in (B) is corresponding FFT image. (C) HAADF STEM image and corresponding elemental mappings. (D) Mo/Ni molar ratios in the dotted-box areas in (C).
Mo/Ni molar ratio from EDX results on the surface region is 0.66 and lower than that of the core region (0.97), indicating the dissolution of Mo-species.

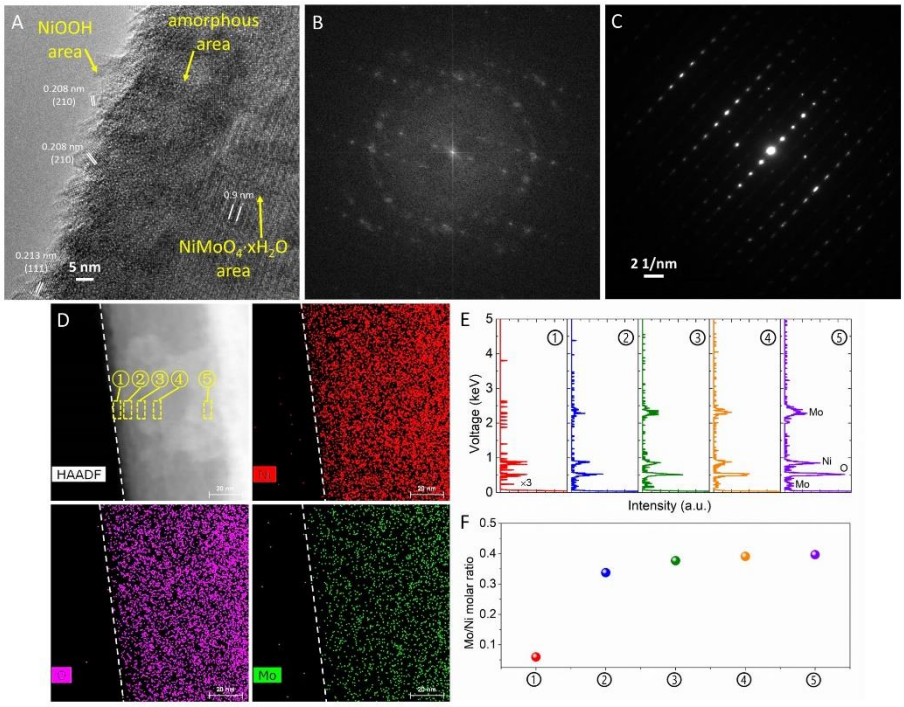

Figure S8. Characterizations on the intermediate product after first-cycle CV to 1.60 V_{RHE} based on $NiMoO_4 \cdot xH_2O$ (also see in Figure 3E). (A) HRTEM image. (B) The corresponding FFT image showing two sets of diffraction. (C) SAED pattern. (D) HAADF STEM image and the

corresponding elemental mappings of the intermediate product after first-CV cycle to 1.60 V_{RHE}. (E) EDX spectra in the five dotted-box areas in (D) and (F) the corresponding Mo/Ni molar ratios, showing the Mo is gradually distributed.
Two sets of diffraction patterns from the corresponding FFT image indicate the existence of second phase. However, only a set of diffraction pattern is visible in the SAED pattern, which may due to the thin-layer NiOOH.

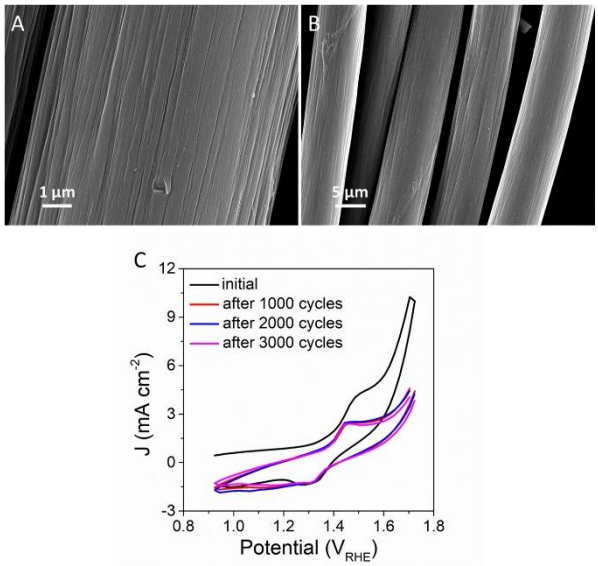

Figure S9. (A, B) SEM images of carbon cloth after long-term CV measurement in 1 M KOH with adding trace of Ni^{2+} salt. (C) The recorded CV curves.
The carbon cloth shows almost no OER activity during CV cycles, indicating that the Ni-species would not deposit on the carbon cloth during such testing condition.

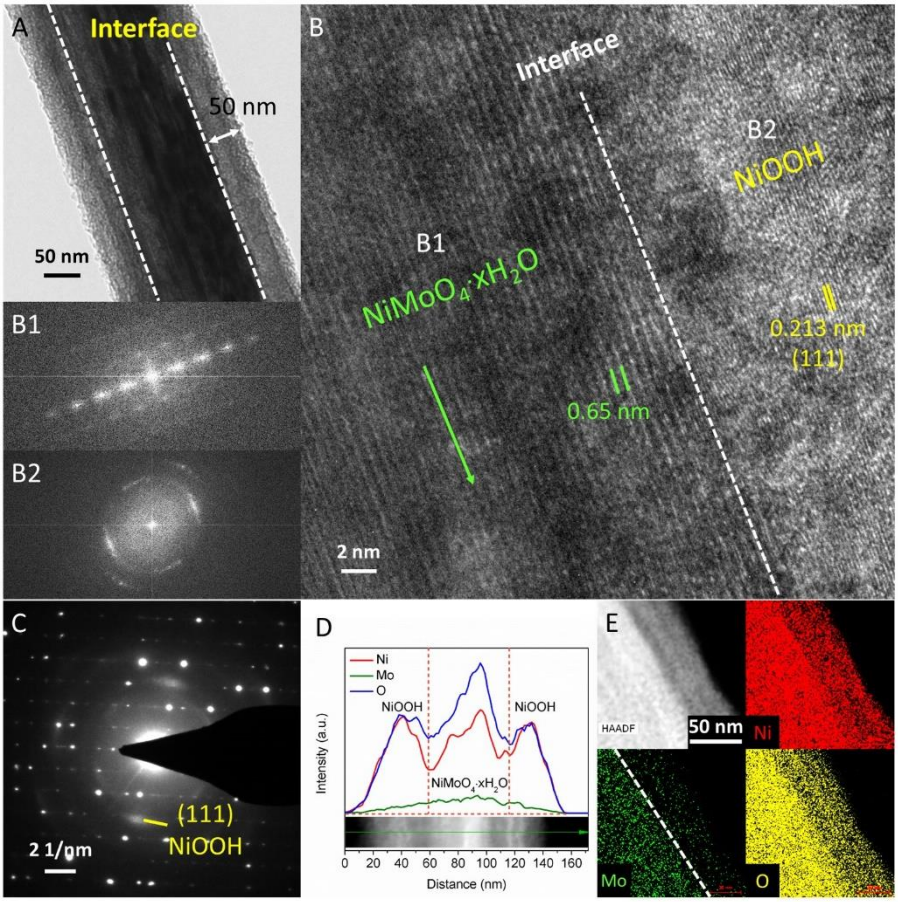

Figure S10. Characterizations on the intermediate product after first-cycle CV based on $NiMoO_4 \cdot xH_2O$ nanowire (also see in Figure 3F). (A) TEM and (B) HRTEM images. (B1, B2) The corresponding FFT images from (B). (C) SAED pattern and (D) the line-scan profiles across an individual nanowire. (E) HAADF STEM image and corresponding elemental mappings.

Two sets of diffraction patterns are visible in SAED, in which the spots are indexed to $NiMoO_4 \cdot xH_2O$ and the polycrystalline rings represent NiOOH. From linear scan analysis along the radial direction of the nanowire, the Ni and O elements exist the whole nanowire but the Mo mainly distribute in the middle of nanowire.

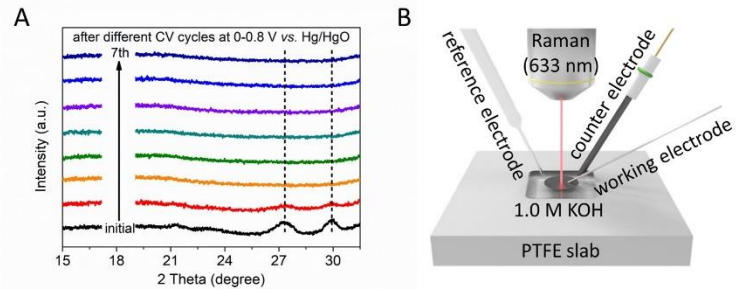

Figure S11. (A) Ex situ XRD patterns of $NiMoO_4 \cdot xH_2O$ NWs/NF after different CV cycles at 50 mV s^{-1}. (B) Schematic illustration of the Raman-electrochemistry coupling system for in situ Raman measurements.

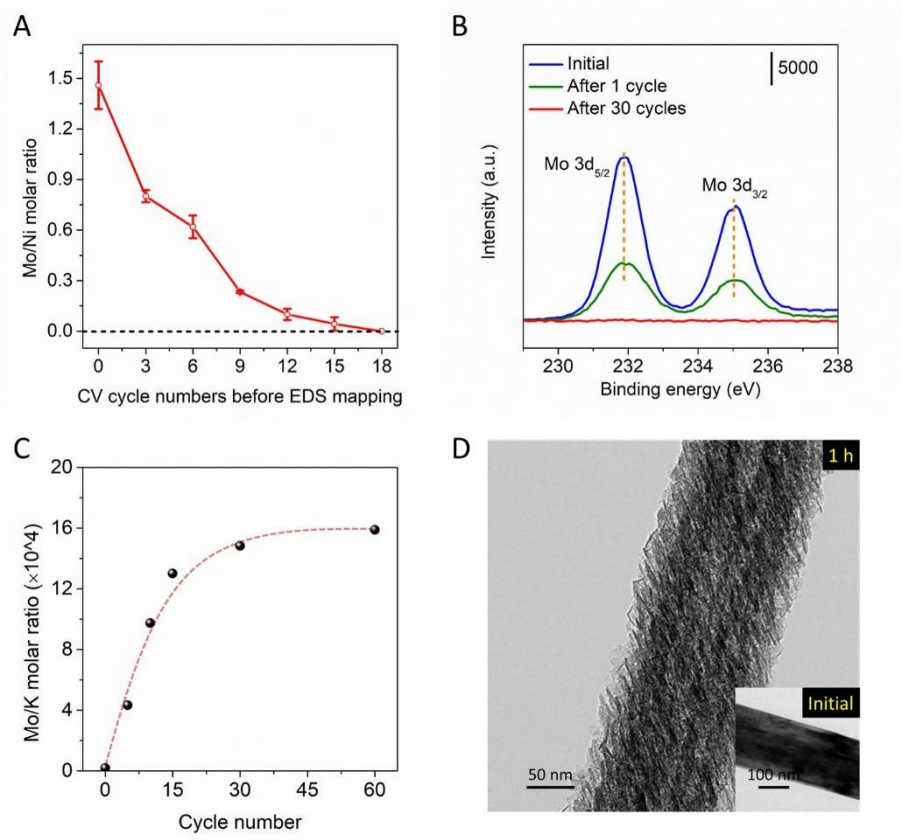

Figure S12. (A) Mo/Ni molar ratios of $NiMoO_4 \cdot xH_2O$ after different CV cycles at 0-0.8 $V_{Hg/HgO}$. (B) High-resolution XPS of Mo 3d for $NiMoO_4 \cdot xH_2O$ initially, after 1-cycle, and 30-cycle CV measurements. (C) ICP results, showing the Mo/K molar ratios in 1 M KOH after different CV cycles tested at 50 mV s^{-1} in 0-0.8 $V_{Hg/HgO}$ based on $NiMoO_4 \cdot xH_2O$ array electrode. (D) TEM images of (inset) initial $NiMoO_4 \cdot xH_2O$ nanowire and etched $Ni(OH)_2$ nanowire with nanosheet-assembled structure.

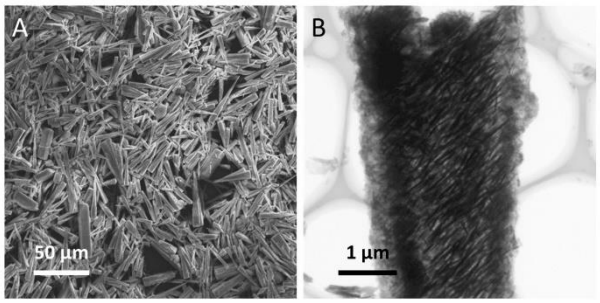

Figure S13. (A) SEM image of Fe-doped $CoMoO_4 \cdot 0.75H_2O$ and (B) TEM image of its product after alkali etching.

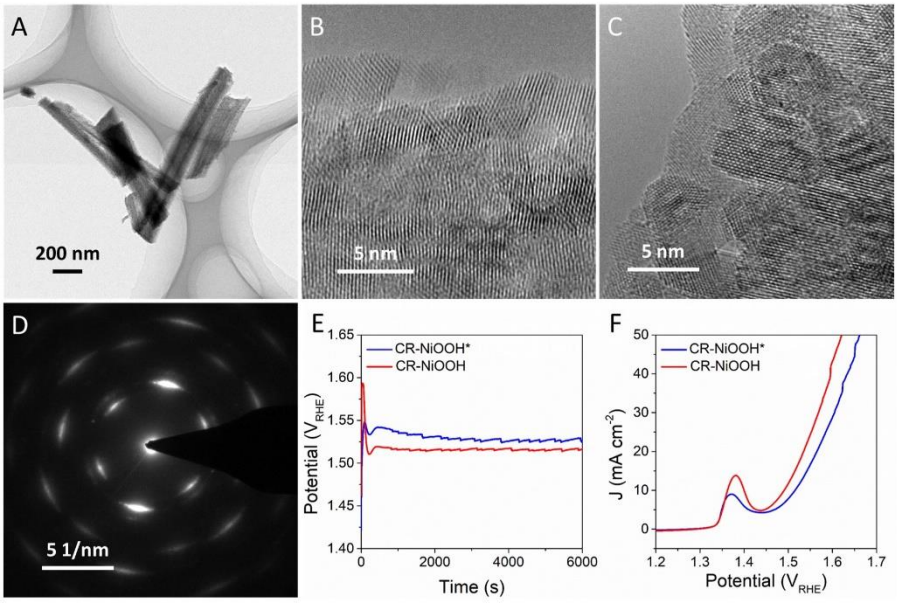

Figure S14. (A) TEM and (B) HRTEM images of CR-NiOOH*. (C) HRTEM image and (D) SAED pattern of $Ni(OH)_2$ nanosheets, which are derived from the alkali etching of $NiMoO_4 \cdot xH_2O$. (E) Chronopotentiometric measurements at 10 mA cm^{-2} of $NiMoO_4 \cdot xH_2O$ and $Ni(OH)_2$ which is derived from the alkali etching of $NiMoO_4 \cdot xH_2O$, respectively. Here, after 6000 s testing, the $NiMoO_4 \cdot xH_2O$ can completely reconstruct to NiOOH (CR-NiOOH) and $Ni(OH)_2$ can evolve to CR-NiOOH* under continuous OER testing. (F) LSV curves of samples after chronopotentiometric measurements in (E).

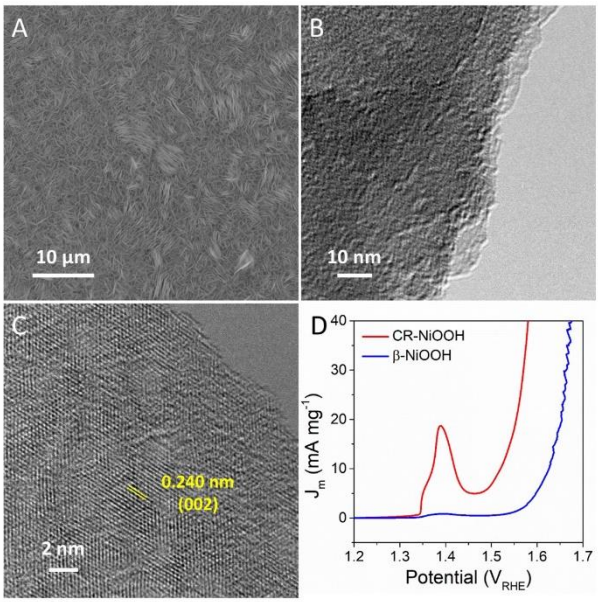

Figure S15. (A) SEM image of $Ni(OH)_2$ nanosheet arrays grown on the nickel foam. (B) TEM and (C) HRTEM images of β-NiOOH derived from $Ni(OH)_2$ after electro-oxidation in 1 M KOH. (D) iR-compensated OER polarization curves of β-NiOOH and CR-NiOOH derived from $NiMoO_4 \cdot xH_2O$.

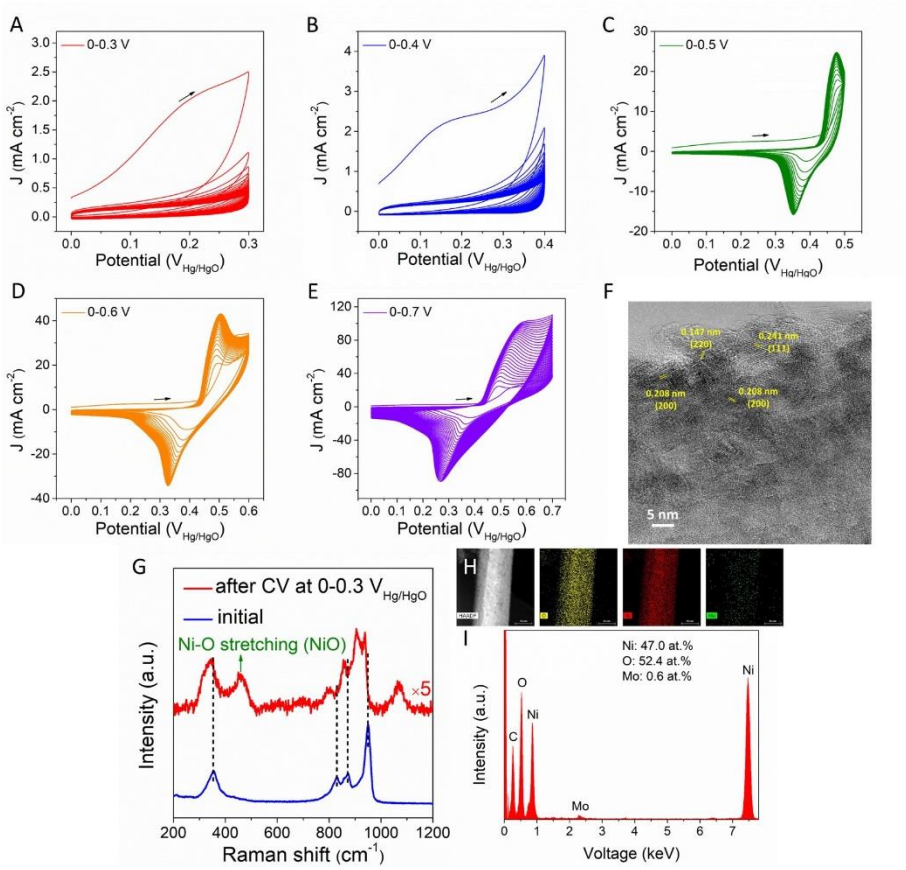

Figure S16. CV curves of $NiMoO_4 \cdot xH_2O$ NWs/NF measured in (A) 0-0.3 V, (B) 0-0.4 V, (C) 0-0.5 V, (D) 0-0.6 V and (E) 0-0.7 $V_{Hg/HgO}$ at 50 mV s^{-1} for 30 cycles. (F) HRTEM image of $NiMoO_4 \cdot xH_2O$ after CV measurements in (A). (G) Raman spectra of $NiMoO_4 \cdot xH_2O$ initially and after CV measurements in (A). (H) HAADF STEM image and corresponding elemental mappings as well as (I) EDX spectrum.

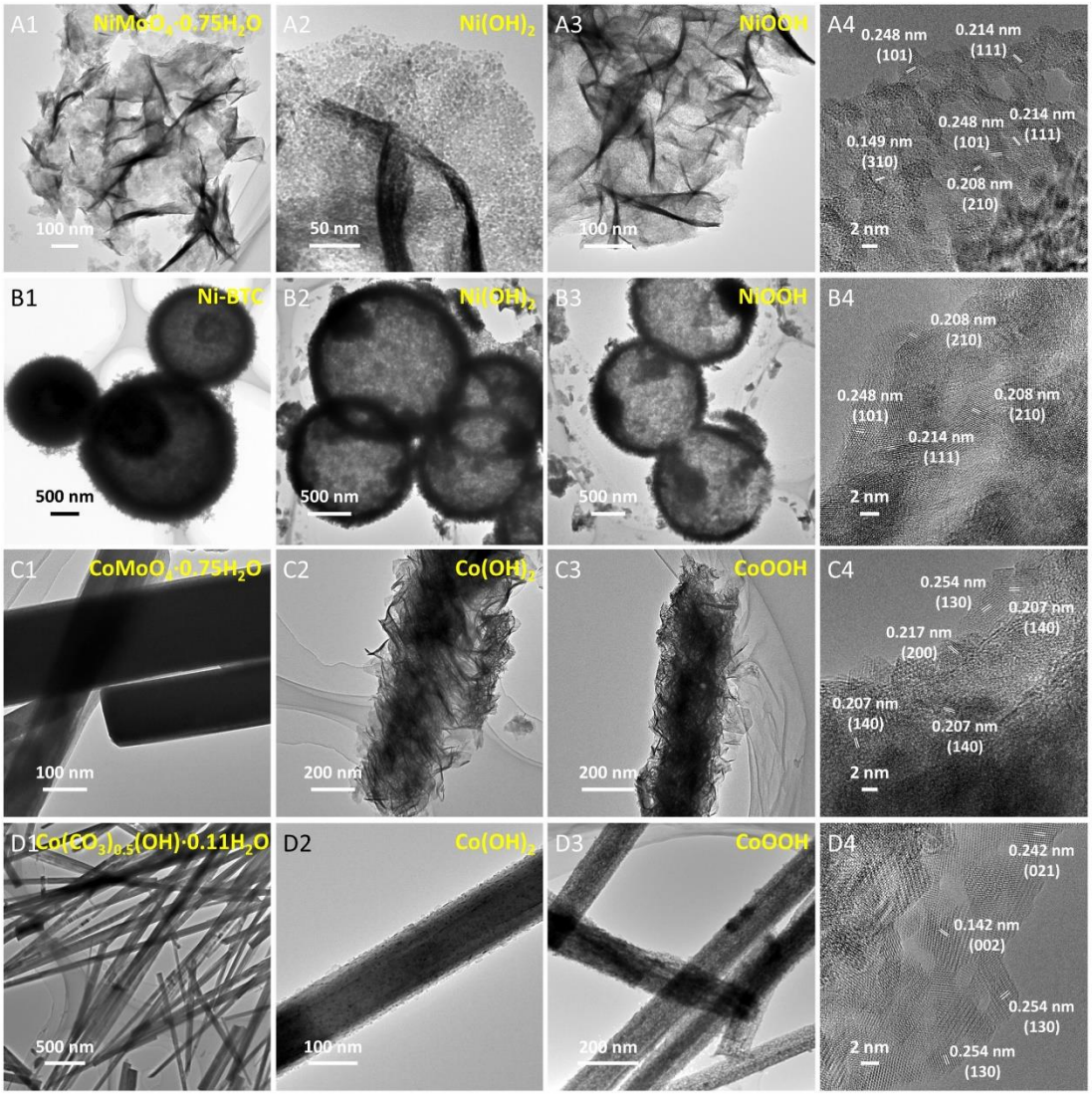

Figure S17. TEM images of (A1) $NiMoO_4 \cdot xH_2O$ nanosheets and (A2) its product after soaking in 1 M KOH for 2 h. (A3) TEM and (A4) HRTEM images of CR-NiOOH nanosheets. TEM images of (B1) Ni-NTC microspheres and (B2) its product after soaking in 1 M KOH for 12 h. (B3) TEM and (B4) HRTEM images of CR-NiOOH microspheres. TEM images of (C1) $CoMoO_4 \cdot 0.75H_2O$ nanowires and (C2) its product after soaking in 1 M KOH for 10 min. (C3) TEM and (C4) HRTEM images of CR-CoOOH nanowires. TEM images of (D1) $Co(CO_3)_{0.5}(OH) \cdot 0.11H_2O$ nanowires and (D2) its product after soaking in 1 M KOH for 2 h. (D3) TEM and (D4) HRTEM images of CR-CoOOH nanowires.

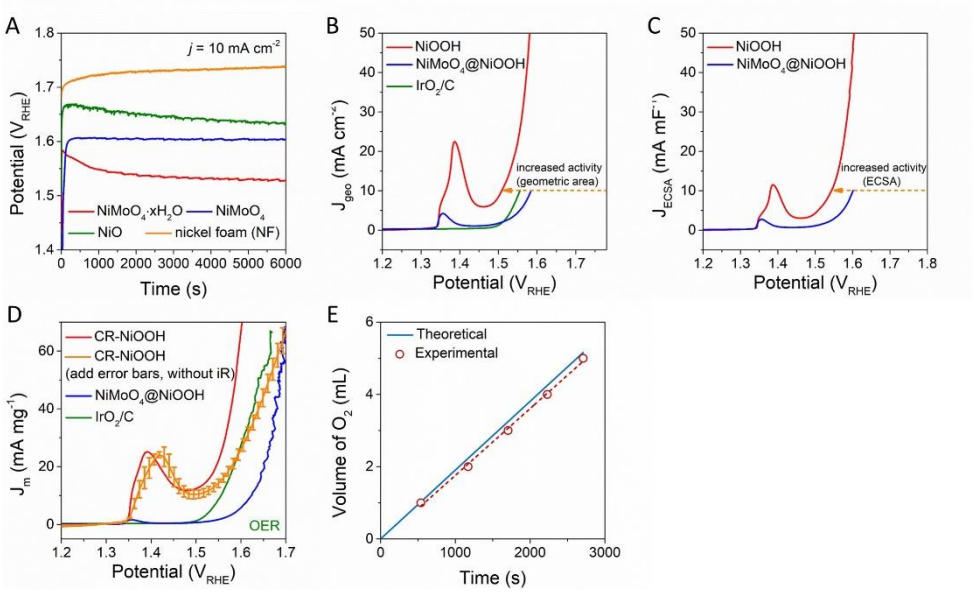

Figure S18. (A) Chronopotentiometric measurements of catalysts at 10 mA cm^{-2}, which reflects the potential change from initial to steady state. iR-compensated OER polarization curves normalized by (B) geometric area, (C) ECSA, and (D) mass at a scan rate of 0.5 mV s^{-1}. (E) Experimental gas evolution during OER and theoretical amount of gas based on CR-NiOOH electrode.

The elementary evolution steps for $NiMoO_4 \cdot xH_2O$ in alkaline solution are depicted as follows:

$$NiMoO_4 \cdot xH_2O + 3OH^- \rightarrow NiOOH + MoO_4^{2-} + (x+1)H_2O + e^- \quad (1)$$

$$NiOOH + OH^- \leftrightarrow NiO(OH)_2 + e^- \quad (2)$$

$$NiO(OH)_2 + 2OH^- \leftrightarrow NiO_2 + 2H_2O + 2e^- \quad (3)$$

$$NiO_2 + OH^- \rightarrow NiOOH + O_2 \uparrow + e^- \quad (4)$$

$$\text{Summary of } (2) - (4): 4OH^- \rightarrow 2H_2O + O_2 \uparrow + 4e^-$$

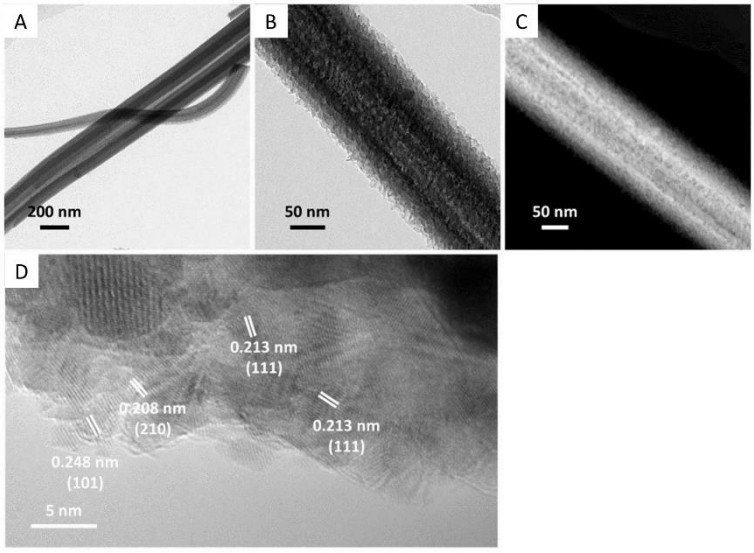

Figure S19. (A, B) TEM, (C) HAADF STEM, and (D) HRTEM images of CR-NiOOH after long-term stability test.

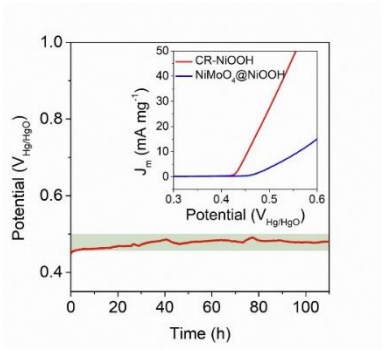

Figure S20. Chronopotentiometric measurements of CR-NiOOH at 10 mA cm^{-2} for UOR. Inset: iR-compensated UOR polarization curves of CR-NiOOH and $NiMoO_4$@NiOOH catalysts normalized by mass.

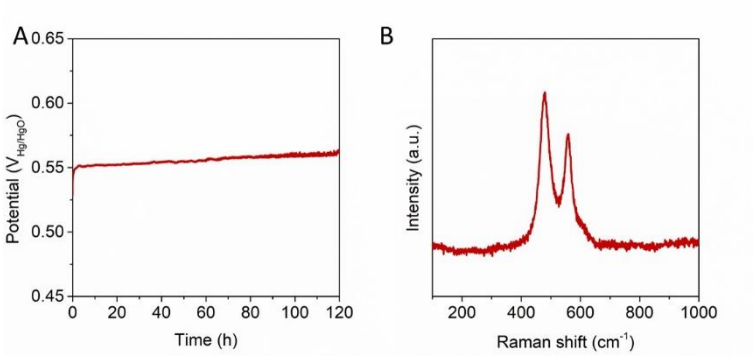

Figure S21. Evaluating CR-NiOOH in 1 M KOH at 52.4°C. (A) Chronopotentiometric measurement of CR-NiOOH at 10 mA cm^{-2}. (B) Raman spectrum of CR-NiOOH after OER durability.

As shown in **Figure S21A**, the CR-NiOOH can provide a stable OER catalysis at 52.4°C for 120 h, with the overpotential increase of only ~10 mV. Besides, two peaks centered at 474 and 554 cm^{-1} which belong to NiOOH are observed in Raman spectrum for CR-NiOOH after such a stability test (**Figure S21B**). These results suggest the excellent phase and catalytic stability of CR-NiOOH during high-temperature OER catalysis.

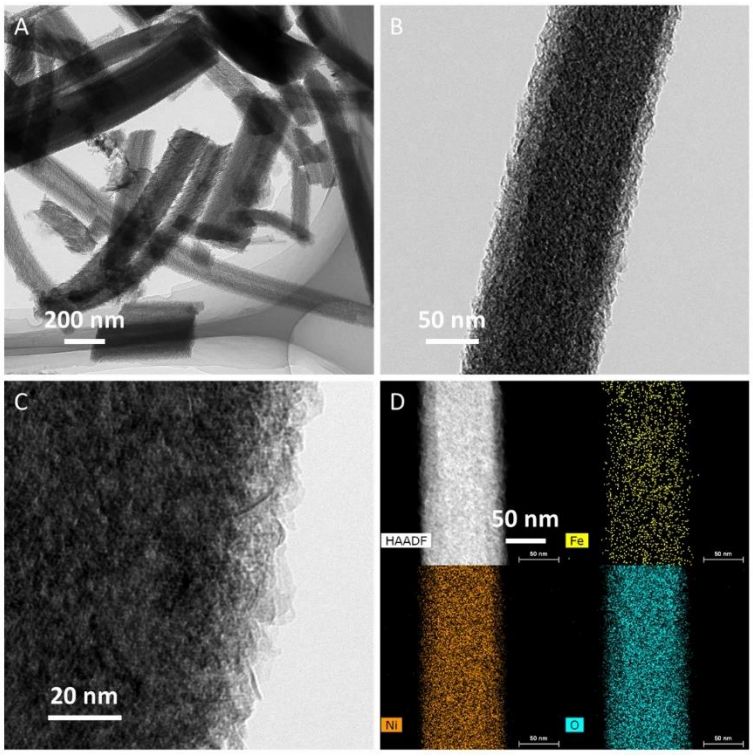

Figure S22. (A-C) TEM and (D) HAADF STEM images and the corresponding elemental mappings of Fe-NiOOH (molar ratio of Fe/Ni is 0.076) after long-term stability test in 30 wt.% KOH.

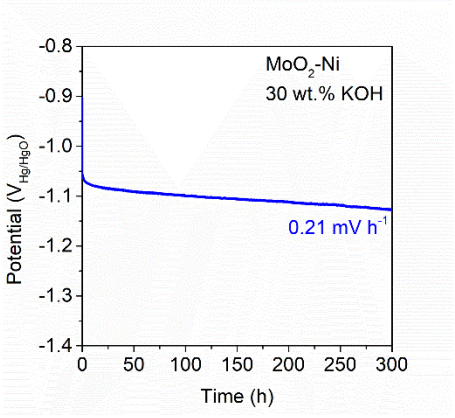

Figure S23. Chronopotentiometric measurements of MoO_2-Ni arrays at -10 mA cm^{-2} in 30 wt.% KOH for HER.

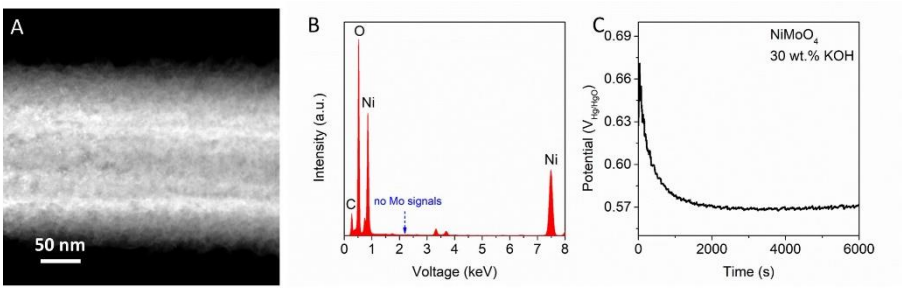

Figure S24. Evaluating $NiMoO_4$ pre-catalyst in industrial 30 wt.% KOH. (A) HAADF STEM image and (B) the corresponding EDX spectrum after measurement in 30 wt.% KOH. (C) The recorded chronopotentiometric measurement of $NiMoO_4$/NF at 10 mA cm^{-2}.

Table S1. Summary of the representative Co/Ni/Fe/Mn-based electrocatalysts and their surface components after activation during OER.

Catalysts	**Partial reconstructed species on the surface**	**References**
NiO	NiOOH and $Ni(OH)_2$	Jpn. J. Appl. Phys. 2009, 48, 015501
$NiCr_2O_4$	Amorphous NiOOH	Chem. Commun. 2018, 54, 4987-4990
Ni_2P	NiOOH	Chem. Mater. 2017, 29, 8539-8547
Ni_3N	NiOOH	J. Am. Chem. Soc. 2015, 137, 4119-4125
Ni_3S_2	Amorphous $Ni(OH)_x$	Nanoscale, 2018, 10, 17347-17353
Ni-P	Nickel oxides/hydroxides	Energy Environ. Sci. 2016, 9, 1246-1250
Ni_3S_2/Ni	Hydrated nickel oxide	Energy Environ. Sci. 2013, 6, 2921-2924
Ni/Ni_xM_y (M = P, S)	Ni oxide species	Adv. Funct. Mater. 2016, 26, 3314-3323
Ni_5P_4	NiOOH	Angew. Chem. Int. Ed. 2015, 54, 12361-12365
TiN@Ni_3N	NiOOH	J. Mater. Chem. A 2016, 4, 5713-5718
NiS	NiOOH	Chem. Commun. 2016, 52, 1486-1489
Ni_3N	Ni hydrate/hydroxide	J. Mater. Chem. A 2015, 3, 8171-8177
Ni_2P	NiO_x	Chem. Commun. 2015, 51, 11626-11629
$Ni_2P_4O_{12}$	Hydroxide	Adv. Mater. 2018, 30, 1705045
Ni_2P	Nickel oxides/hydroxides/oxyhydroxides	ACS Catal. 2016, 6, 714-721
Ni_xB	NiO_x	Adv. Energy Mater. 2017, 7, 1700381
Fe-doped nickel phosphate	NiOOH	Chem. Mater. 2016, 28, 5659-5666
Ni_2P	NiO_x	Energy Environ. Sci. 2015, 8, 2347-2351
CP@Ni-P	$NiO/Ni(OH)_x$	Adv. Funct. Mater. 2016, 26, 4067-4077
Co_4N	CoO_x	Angew. Chem. Int. Ed. 2015, 127, 14923-14927
NiSe	NiOOH	Angew. Chem. Int. Ed. 2015, 127, 9483-9487
Nickel sulfide	Nickel oxides	Adv. Energy Mater. 2016, 6, 1502333
FeP/Ni_2P	Nickel and iron oxides/oxyhydroxides	Nat. Commun. 2018, 9, 2551
Nickel–iron disulfide	Ni(Fe)OOH	J. Mater. Chem. A 2017, 5, 4335-4342
Mn_3N_2	MnO_x	Angew. Chem. Int. Ed. 2017, 130, 706-710
$Ba_{0.5}Sr_{0.5}Co_{0.8}Fe_{0.2}O_{3-\delta}$	Metal oxy(hydroxide)	Nat. Mater. 2017, 16, 925-931

Table S2. Summary of the reconstruction results between the reconstruction layer thicknesses (RLt) and the smallest size of OER pre-catalyst in one dimension in our work and previous works.

Catalysts	**The smallest size in one dimension (nm)**	**Rlt (nm)**	**References**
$NiMoO_4 \cdot xH_2O$ nanowires	200	200	This work
$Co(CO_3)_{0.5}(OH) \cdot 0.11H_2O$ nanowires	150	150	
$NiMoO_4$ nanowires	200	7	
Boronized Ni	8700 (For convenience, the value of 300 is shown in Figure 1)	2-5	Energy Environ. Sci. 2019, 12, 684-692
Ni_3Se_2 nanoparticles	~200	4-5	ACS Catal. 2017, 7, 310-315
NiSe nanoparticles	250	4-6	
NiO nanoparticles	~100	7-8	
FeB_2 nanoparticles	20-50	~15	Adv. Energy Mater. 2017, 7, 1700513
Ultrathin FeSe nanosheets	15	15	J. Am. Chem. Soc. 2019, 141, 7005-7013
Ni_2P particles	~50	~10	Energy Environ. Sci. 2015, 8, 2347-2351
Co_3C particles	20-30	20-30	ACS Appl. Energy Mater. 2018, 1, 5145, 5150
F-incorporating NiFe hydroxide nanosheets	100	~35	Nano Lett. 2019, 19, 530-537
Ni_2P hollow microspheres	13-19	~8	Chem. Mater. 2017, 29, 8539-8547
$Co_2(OH)Cl$ nanoparticles	~10	10	Adv. Mater. 2019, 31, 1805127
$LaFe_{0.2}Ni_{0.8}O_3$ nanorods	37	4	Angew. Chem. Int. Ed. 2015, 127, 2338-2342
La_2NiMnO_6 nanoparticles	~33	5-8	J. Am. Chem. Soc. 2018, 140, 11165-11169
Co_4N nanowires	~100	5-10	Angew. Chem. Int. Ed. 2015, 127, 14923-14927
Ni_3C/C nanoparticles	20-50	8	ACS Energy Lett. 2019, 4, 2585-2592
Lithiated NiO nanoparticles	5	5	
Ni nanoparticles	~100	~5	Adv. Mater. 2016, 28, 3326-3332
Ni-Fe disulfide microspheres	~75	~10	J. Mater. Chem. A 2017, 5, 4335-4342
Ultrathin Ni-Fe LDH nanosheets	1.2	1.2	ACS Catal. 2019, 9,6027-6032

Table S3. Comparison of recently reported AWE performance based on coupled (or bifunctional) catalysts tested in 1 M KOH.

Anode//cathodic catalysts	AWE performance	Stability	References
Fe-NiOOH/NF//MoO_2-Ni/NF	1.48 V at 10 mA cm^{-2}	580 h at 10 mA cm^{-2}	This work
$Ni_{11}(HPO_3)_8(OH)_6$	1.65 V at 10 mA cm^{-2}	100 h at 1.65 V	Energy Environ. Sci. 2018, 11, 1287-1298
NiFe LDH@NiCoP/NF	1.57 V at 10 mA cm^{-2}	100 h at 10 mA cm^{-2}	Adv. Funct. Mater. 2018, 28, 1706847
CoNi@NC-600	1.678 V at 10 mA cm^{-2}	19.44 h at 10 mA cm^{-2}	Nano Lett. 2017, 17, 7773-7781
LSC&$MoSe_2$ (LSC: $La_{0.5}Sr_{0.5}CoO_{3-\delta}$)	2.3 V at 100 mA cm^{-2}	1000 h at 100 mA cm^{-2}	Nat. Commun. 2019, 10, 1723
Cr-doped FeNi–P/NCN (NCN: N-doped carbon nanotubes)	1.50 V at 10 mA cm^{-2}	20 h at 10 mA cm^{-2}	Adv. Mater. 2019, 31, 1900178
Co@N-CS/N-HCP@CC (N-CS: N-doped carbon nanosheets; N-HCP: N-doped hollow carbon polyhedra)	1.545 V at 10 mA cm^{-2}	24 h at 30 mA cm^{-2}	Adv. Energy Mater. 2019, 9, 1803918
Cu@NiFe LDH/Cu foam	1.54 V at 10 mA cm^{-2}	48 h at 10 mA cm^{-2}	Energy Environ. Sci. 2017, 10, 1820-1827
FeP/Ni_2P/NF	1.42 V at 10 mA cm^{-2}	~40 h at 30 mA cm^{-2}	Nat. Commun. 2018, 9, 2551

Table S4. Comparison of reported catalytic performance of catalysts tested in industrial-concentration alkali.

Catalysts	Performance	References
Fe-NiOOH/NF	~0.5 V vs. Hg/HgO at 10 mA cm^{-2} for 210 h (OER, 30 wt.% KOH); ~1.63 V at 10 mA cm^{-2} for 260 h (AWE, 30 wt.% KOH, coupled with MoO_2-Ni cathode)	This work
DR-NiOOH/NF	~0.54 V vs. Hg/HgO at 10 mA cm^{-2} for 72 h (OER, 30 wt.% KOH)	ACS Energy Lett. 2019, 4, 2585-2592
$Co_{15}Ni_{30}Mo_{55}$	39.81 mA cm^{-2} at overpotential of 400 mV (OER, 30 wt.% KOH)	ECS Trans. 2006, 3, 135-148
NiFe-OOH/NF	~300 mA cm^{-2} at 1.6 V vs. RHE (OER, 30 wt.% KOH)	Mater. Chem. Front. 2017, 1, 2541-2546
$Fe_{11.8\%}$-Ni_3S_2/NF	~500 mA cm^{-2} at overpotential of 238 mV for 14 h (OER, 30 wt.% KOH)	J. Mater. Chem. A 2015, 3, 23207-23212
Ni-Fe-OH@Ni_3S_2/NF	~1.65 V vs. RHE at 1000 mA cm^{-2} for 50 h (OER, 30wt.% KOH)	Adv. Mater. 2017, 29, 1700404
Fe-NiSe/FeNi foam	~1.44 V vs. RHE at 100 mA cm^{-2} for 20 h (OER, 30wt.% KOH)	Chem. Commun. 2016, 52, 4529-4532
NiO with O-vacancies (NiO-O_v)	~1.64 V at 10 mA cm^{-2} for 20 h (AWE, 6 M KOH, coupled with NiO-O_v cathode)	Nano Energy 2018, 43, 103-109
NiFe-LDH	~1.63 V vs. RHE at 1000 mA cm^{-2} for 1050 h (OER, 10 M KOH)	Nat. Commun. 2018, 9, 2609
Ni-MOF	~1.45 V vs. RHE at 10 mA cm^{-2} for 12 h (OER, 30 wt.% KOH)	ChemElectroChem 2018, 5, 2795-2807